APPLIED SCIENCES AND ENGINEERING

Cell invasion in digital microfluidic microgel systems

Bingyu B. Li[1,2], Erica Y. Scott[1,2,3], M. Dean Chamberlain[1,2,3], Bill T. V. Duong[1,2,3], Shuailong Zhang[1,2,3], Susan J. Done[4,5], Aaron R. Wheeler[1,2,3]*

Microfluidic methods for studying cell invasion can be subdivided into those in which cells invade into free space and those in which cells invade into hydrogels. The former techniques allow straightforward extraction of subpopulations of cells for RNA sequencing, while the latter preserve key aspects of cell interactions with the extracellular matrix (ECM). Here, we introduce "cell invasion in digital microfluidic microgel systems" (CIMMS), which bridges the gap between them, allowing the stratification of cells on the basis of their invasiveness into hydrogels for RNA sequencing. In initial studies with a breast cancer model, 244 genes were found to be differentially expressed between invading and noninvading cells, including genes correlating with ECM-remodeling, chemokine/cytokine receptors, and G protein transducers. These results suggest that CIMMS will be a valuable tool for probing metastasis as well as the many physiological processes that rely on invasion, such as tissue development, repair, and protection.

INTRODUCTION

Cell invasion from one tissue into another is a fundamental process found in pathologies such as cancer as well as in homeostatic processes such as tissue development and repair (*1*). A host of in vitro assay techniques have been developed to evaluate this process, which can be subcategorized in terms of their format: (i) methods in which cells invade into free (fluid-filled) space and (ii) methods in which cells invade into a three-dimensional (3D) hydrogel that mimics the extracellular matrix (ECM).

The classic example of a type 1 in vitro invasion assay tool is the Boyden chamber (*2*), in which cells invade (vertically) from a top to a bottom chamber separated by a porous membrane. There are a number of microfluidic systems that have been developed that mimic the Boyden chamber, in which cells invade (horizontally) into open microchannels (*3*–*6*). Unlike the Boyden chamber, these methods permit high-resolution microscopy imaging that is only possible in the horizontal dimension. But the most important feature of type 1 assays is that it is straightforward to collect the cells after invasion for analysis by RNA sequencing (RNA-seq), which has emerged as an indispensable tool for understanding disease progression and identifying novel biomarkers (*7*). The disadvantage of type 1 methods is that they are blind to ECM remodeling—a complex process that includes the formation of physical protrusions, application of mechanical stresses via cell-ECM adhesion, exposure to matrix-digesting proteases for localized proteolysis, and the releasing of adhesion bonds at the trailing ends of invaded cells (*8*). Matrix remodeling is particularly important in the first stages of metastasis (*9*), making it a critical area of study for the development of new anticancer therapies and interventions.

The classic example of a type 2 in vitro invasion assay tool is the hydrogel invasion assay (*10*), in which cells invade (vertically) into hydrogels immobilized in a well plate. There are also a number of microfluidic systems that have been developed that mimic the hydrogel invasion assay, in which cells invade (horizontally) into microchannels filled with 3D ECM-like material (*11*–*16*). Like the type 1 microfluidic tools, type 2 tools also allow for high-resolution microscopy in the horizontal dimension. The primary advantage of type 2 microfluidic systems is the capacity to observe ECM remodeling. A critical drawback of these methods, however, is the complexity of extracting cells from the matrix for analysis by RNA-seq. We are not aware of previous reports of a type 2 system with this capability.

In response to the challenges outlined above, we introduce a type 2 invasion assay platform that we call cell invasion in digital microfluidic microgel systems (CIMMS). CIMMS relies on an alternate form of microfluidics known as digital microfluidics (DMF), which has emerged as a powerful platform for cell culture and analysis, including 3D cell culture models (*17*–*20*). CIMMS joins the existing microchannel-based type 2 invasion assay platforms in providing access to complex, multimaterial, in vivo–like systems that are integrated with high-resolution microscopy and imaging. But uniquely, CIMMS combines type 2 invasion assays with the capacity to isolate subpopulations of invading cells for analysis by RNA-seq. Given the ubiquity of invasion and matrix remodeling in living systems, we propose that this combination will prove important for improving our understanding of these complex processes.

RESULTS

Cell invasion in digital microfluidic microgel systems

In initial work, we used CIMMS to recapitulate the breast cancer tumor microenvironment (Fig. 1A), but we propose that it is a general strategy that might be applied to many different systems. CIMMS relies on the capacity for DMF to precisely form submillimeter-sized hydrogels or "microgels" (Fig. 1, B and C). In this study, microgels were typically formed with a collagen I core surrounded by an encapsulating shell of basement membrane extract (BME) (i.e., a "core-shell" microgel); "simple" microgels (containing only collagen I or BME) were also used. All the droplet manipulation steps required for microgel formation, cell seeding, and invasion are automated using the open-source DropBot control system (http://microfluidics.utoronto.ca/dropbot/).

[1]Institute for Biomaterials and Biomedical Engineering, University of Toronto, 164 College St., Toronto, ON M5S 3G9, Canada. [2]Donnelly Centre for Cellular and Biomolecular Research, University of Toronto, 160 College St., Toronto, ON M5S 3E1, Canada. [3]Department of Chemistry, University of Toronto, 80 St. George St., Toronto, ON M5S 3H6, Canada. [4]Laboratory Medicine Program, University Health Network, 200 Elizabeth St., Toronto, ON M5G 2C4, Canada. [5]Department of Laboratory Medicine and Pathobiology, University of Toronto, 1 King's College Circle, Toronto, ON M5S 1A1, Canada.
*Corresponding author. Email: aaron.wheeler@utoronto.ca

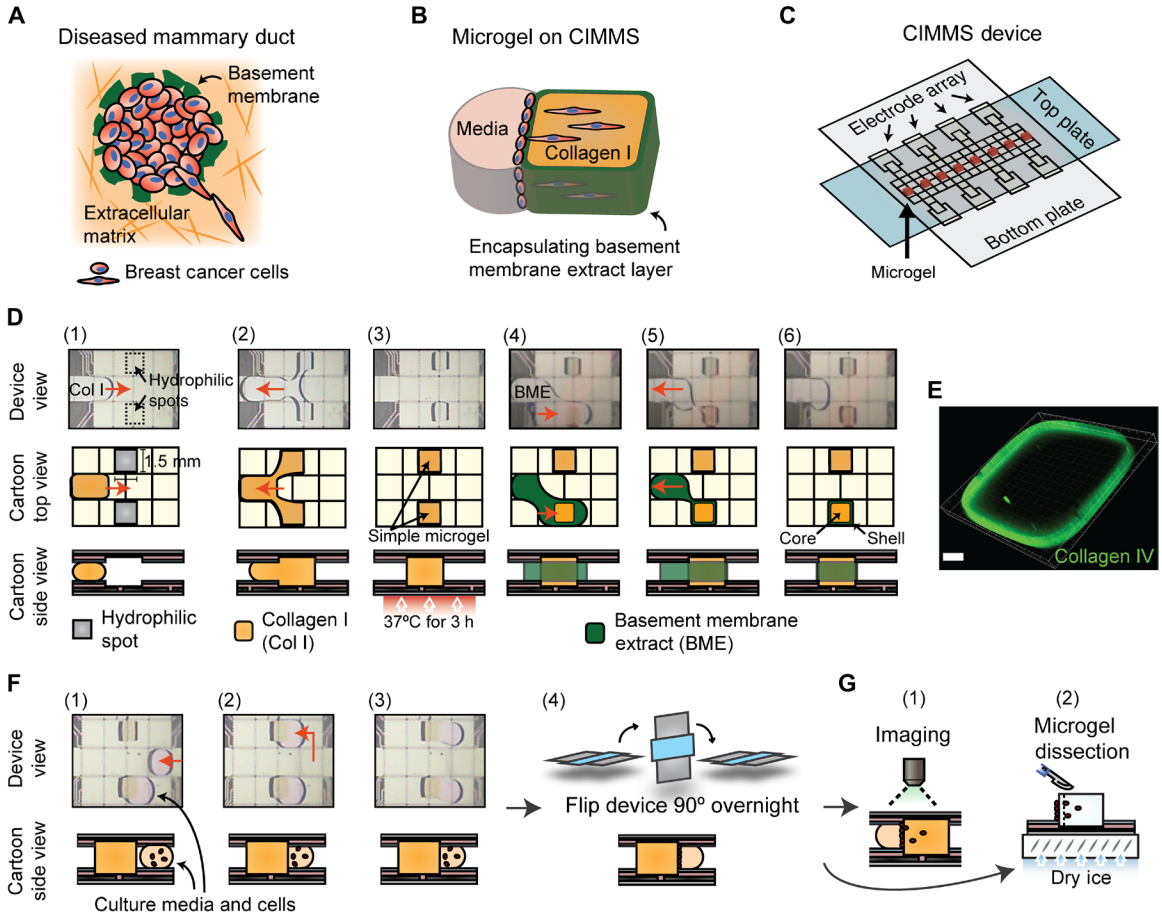

Fig. 1. CIMMS. (**A**) Cartoon of the first step of breast cancer metastasis from the mammary duct, in which tumor cells (red) breach the disrupted basement membrane (green) and invade the collagen-rich ECM (orange). (**B**) Cartoon of a core-shell microgel generated by CIMMS to mimic (A). (**C**) Schematic of a CIMMS device designed to generate eight microgels. (**D**) Photos (top) and cartoons (bottom) depicting the formation of core-shell microgels in situ. (1 to 3) A droplet of sol-phase collagen I (orange in the cartoons) is actuated across one (or more) 1.5 mm by 1.5 mm hydrophilic site(s) (gray in the cartoons), forming (a) droplet(s) by passive dispensing. The droplet(s) formed in this manner gelled at elevated temperature into one (or more) solid core(s). (4 to 6) A droplet of sol-phase BME (green in the cartoons) is actuated across one or more collagen I core(s) to leave (an) encapsulating shell(s). Red arrows indicate the direction of droplet movement. (**E**) 3D confocal microscopy image of a core-shell microgel immunostained for collagen IV (green). Scale bar, 200 μm. (**F**) Photos (top) and cartoons (bottom) depicting cancer cell seeding in a CIMMS assay. (1 to 3) A droplet of media (pale pink in the cartoons) containing breast cancer cells is actuated to touch the edge of one (or more) microgel(s) (orange in the cartoons), and (4) the device is rotated 90° to allow cells to settle on the edge(s) of the microgel(s) via gravity. Following cell attachment, the device is returned to its regular orientation and "fed" (supplementing old media with fresh media) on day 2. (**G**) On day 4, (1) confocal microscopy is used to generate 3D images of each microgel to determine invasion distance, morphology, and protein expression, and/or (2) microgels can be flash-frozen to excise subpopulations of cells for transcriptomic analysis. All pictures in this figure feature core-shell microgels formed from collagen I (2.4 mg/ml) and 10% BME. Photo credits: B. B. Li, University of Toronto.

To generate core-shell microgels, solution-phase (sol-phase) collagen I droplets were first dispensed onto the actuation electrodes and driven across patterned hydrophilic spots to cause the phenomenon known as passive dispensing (Fig. 1D, panels 1 to 3) (*21*). Passively dispensed droplets were then incubated at elevated temperature to allow for gelation, and basement membrane layers were formed by dispensing droplets of sol-phase BME onto the array and driving them across collagen I microgels to form BME coatings (Fig. 1D, panels 4 to 6). The thickness of the BME shell was found to be controllable by changing the concentration of BME. Two thicknesses were used here, generated from 10% BME (thin shell) or 25% BME (thick shell), which had thicknesses of 3.11 ± 0.35 μm or 4.45 ± 0.64 μm, respectively (average ± 1 SD from $n = 3$ replicates each), determined from fluorescent microscopy after immunofluorescent staining (Fig. 1E). Scanning electron microscopy (SEM) of core-shell microgels formed in this manner features the well-known fibrillized morphology of collagen I core surrounded by a thin, dense layer of BME coating (fig. S1, A to C).

Following formation of microgels, cells were seeded by dispensing droplets of cell culture media containing suspended cells and manipulating them such that each touched one side of a designated microgel (Fig. 1F). Then, the device was rotated 90° to allow cells to settle on one side of the microgel. Last, the device was returned to its original orientation and maintained under standard mammalian cell culture conditions. Two methods were used to analyze cell invasion (Fig. 1G): (i) confocal immunofluorescence microscopy and (ii) microgel dissection and transcriptome analysis.

CIMMS was found to be robust and repeatable, allowing for reproducible dispensing and aliquoting of ~200 to 700 cells to each

microgel depending on seeding density (fig. S1D), and with high viability (>90% on day 4) when coupled with automated media replenishment on day 2 (fig. S1, E and F). Initial work revealed that a method reported previously (*17*) for forming microgels on DMF devices resulted in asymmetric structures not suitable for invasion assays, as cells simply migrated along the (nonplanar) sides of the gels (fig. S2, A and B). Thus, CIMMS required the development of a method in which microgels are anchored to hydrophilic sites on both device substrates (fig. S2C), which results in devices that are reliably capable of forming gels suitable for invasion assays.

As a first step toward evaluating the technique, CIMMS was compared to conventional hydrogel invasion assays. In the latter technique, cells are deposited on top of hydrogels formed in a well plate to observe the invasion into the gel in the (vertical) *z* dimension (Fig. 2A and fig. S3A), with three key limitations. First, microscopy resolution in the *z* axis is limited relative to the *x*-*y* axes that are used to image the invasion in CIMMS (Fig. 2B), which restricts the quality of the morphology information that can be acquired. Second, hydrogels formed in well plates have large, unsupported surface areas, which tend to form rippling topographies with features that range up to 60 μm (Fig. 2, B and C, and fig. S3, B to D). Third, there is a substantial meniscus effect in gels that are cast into wells (that can extend up to 500 μm up the sides of the wells), which complicates the distinction between invading and noninvading populations. Cryosectioning can produce thin slices of the gel to circumvent some of these challenges (Fig. 2C and fig. S3E); however, this technique is labor intensive (*10*) and requires manual measurements to determine invasion distance.

Like type 2 invasion assay systems that rely on microchannels (*11*–*16*), CIMMS solves problems inherent in conventional gel invasion assays. First, as illustrated in Fig. 2D, cell invasion in CIMMS is in the (horizontal) *x*-*y* plane, which allows for high-resolution immunofluorescence imaging (Fig. 2E), as well as the observation of subtle morphological details, e.g., mesenchymal versus ameboid phenotype (fig. S4A) (*9*) that cannot be observed in poorly resolved *z*-axis images. Second, the matrix is mechanically robust, with solid supports on either side of the narrow microgel, a format that is not subject to surface rippling effect found in well plates (fig. S4, B and C). Third, the highly regular dimensions of microgels make automated identification and quantitation of cell invasion distances straightforward in situ (with no need for cryosectioning) (fig. S4, D and E). Overall, CIMMS allows rapid, robust detection of invading versus noninvading cells as well as invasion distances and invading cell morphology.

CIMMS with immunofluorescence imaging

CIMMS was designed to be able to generate high-resolution immunofluorescence confocal images, allowing for detailed quantitative and qualitative analysis of invasion behavior, using an automated (droplet-based) 15-step immunofluorescent staining procedure. To test the former property (quantitative analysis), CIMMS was used to evaluate invasion of MDA-MB-231 cells under a range of different conditions (Fig. 3, A to C), leading to a number of interesting findings. For example, increasing cell seeding density from 200,000/ml to 600,000/ml increased the percentage of cells invaded from 17.3 ± 15.6% to 38.4 ± 16.5% ($P = 0.0008$, $n \geq 15$) and the average invasion distance from 69.5 ± 33.1 μm to 101.5 ± 29.4 μm ($P = 0.0072$, $n \geq 15$), which suggests that invasion is correlated with the confluency of cells on the microgel surface. Increasing collagen I concentration for simple microgels from 1.5 to 2.4 mg/ml resulted in a modest

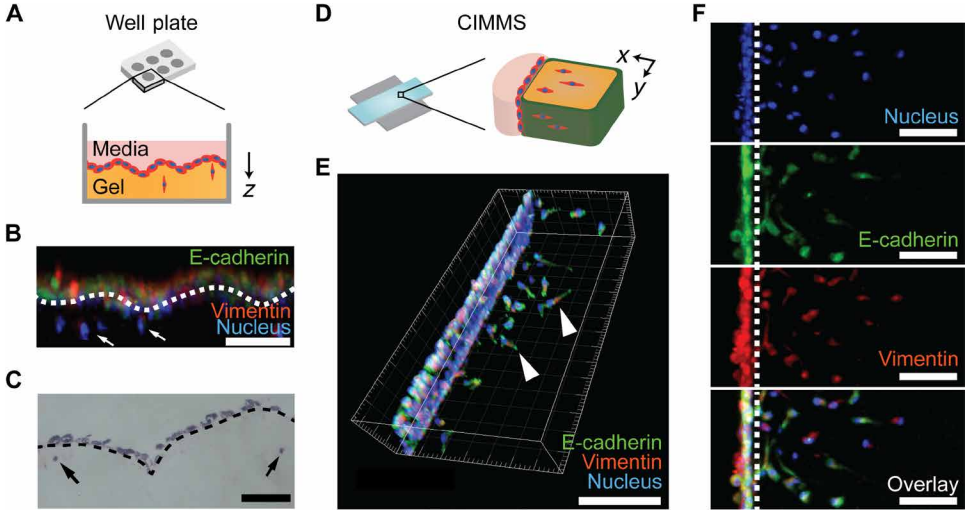

Fig. 2. Comparison of 3D invasion assays in well plates and in CIMMS devices. (**A**) Cartoon of a conventional well plate (top) and zoomed view of a 3D gel invasion assay (bottom). The surface of the collagen I gel (orange) is often uneven, leading to differences in vertical starting positions of the cancer cells (red). (**B**) *Z*-axis confocal image of a cross section of a gel in a well plate with MDA-MB-231 cells (nucleus, blue; E-cadherin, green; and vimentin, red—these colors were used for all immunostained images in this figure) seeded at 100,000/ml on a simple collagen I microgel (2.4 mg/ml) in a well plate on day 4 after seeding. The dotted white line highlights the uneven gel surface, and white arrows indicate invaded cells. Scale bar, 100 μm. (**C**) Hematoxylin and eosin staining of a cryosection of MDA-MB-231 cells under the same conditions as (B). Noninvaded cells are on top of the gel surface (dashed black line), and invaded cells are indicted by black arrows. Scale bar, 100 μm. (**D**) Cartoon of a CIMMS device bearing microgels (left) and zoomed view of a core-shell microgel (right). (**E**) 3D confocal microscopy image of a core-shell microgel [formed from collagen I (2.4 mg/ml) and 10% BME] on day 2 after seeding MDA-MB-231 cells at 400,000/ml, with examples of invaded cells highlighted with white arrowheads. Scale bar, 200 μm. (**F**) Top view (*x*-*y* plane) of confocal 3D image showing MDA-MB-231 cells on day 4 after seeding in a CIMMS device at 400,000/ml and invading into simple collagen I microgels (2.4 mg/ml), immunofluorescently labeled for (top to bottom): nucleus, E-cadherin, vimentin, and an overlay. The white dotted line represents the microgel edge. Scale bar, 100 μm.

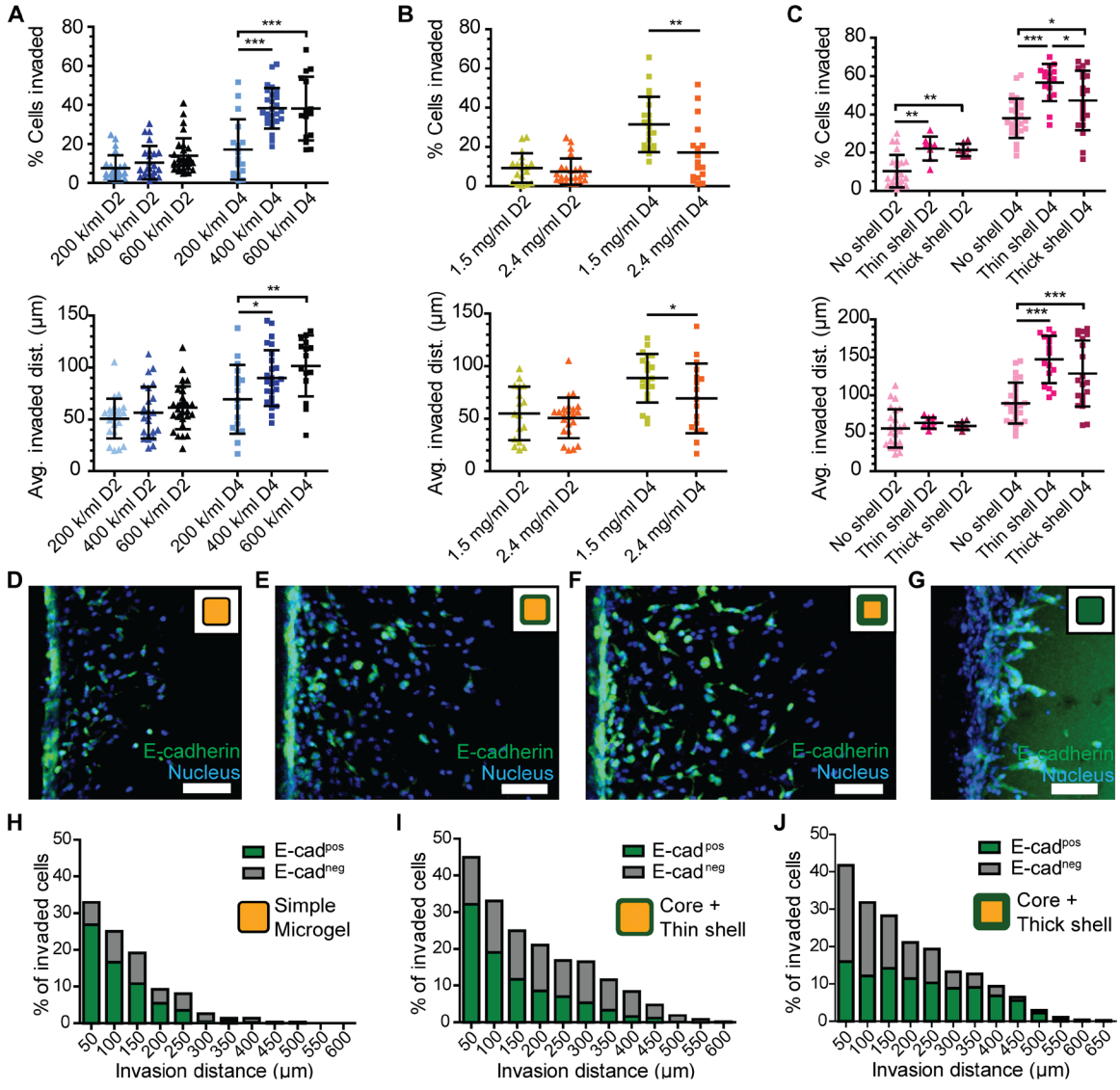

Fig. 3. Image-based analysis of cancer cell invasion assay using CIMMS. (**A** to **C**) Percentages of invading MDA-MB-231 cells (top) and average invasion distance of those that have invaded (bottom) on day 2 (left, triangles) and day 4 (right, squares) after seeding. Error bars represent ±1 SD for $n = 8$ to 30 microgels per condition. (*$P < 0.05$; **$P < 0.01$, and ***$P < 0.001$) (A) Results for cells seeded at different densities (light blue, 200,000/ml; dark blue, 400,000/ml; black, 600,000/ml) on simple microgels formed from collagen I (2.4 mg/ml). (B) Results for cells seeded at 200,000/ml on simple microgels containing collagen I formed from different concentrations (yellow, 1.5 mg/ml; orange, 2.4 mg/ml). (C) Results for cells seeded at 400,000/ml on simple microgels formed from collagen I (light pink; 2.4 mg/ml) and core-shell microgels formed from collagen I (2.4 mg/ml) and 10% BME (dark pink) or 25% BME (burgundy). (**D** to **G**) Representative top view 3D confocal images showing MDA-MB-231 cells on day 4 after seeding at 400,000/ml for (D) a simple microgel formed from collagen I (2.4 mg/ml), (E) a core-thin shell microgel formed from collagen I (2.4 mg/ml) and 10% BME, (F) a core-thick shell formed from collagen I (2.4 mg/ml) and 25% BME, and (G) a simple microgel formed from 50% BME. Cells were immunostained for nucleus (blue) and E-cadherin (green); inset cartoons illustrate the makeup of the microgels. Scale bar, 100 μm (D to G). (**H** to **J**) Plots of the percent of invading MDA-MB-231 cells on day 4 after seeding at 400,000/ml that express (green, E-cad^{pos}) and do not express (gray, E-cad^{neg}) E-cadherin as a function of invasion distance. The percentages shown were calculated from summed cell numbers invading four microgels per condition in (H) simple microgels with the same condition as (D), (I) core-thin shell microgels with the same condition as (E), and (J) core-thick shell microgels with the same condition as (F).

decrease in the percentage of cells invaded, from 31.6 ± 14% to 17.25 ± 16% ($P = 0.006$, $n \geq 17$), likely related to the decreased pore size and higher stiffness associated with gels formed from higher collagen concentration. The presence of a thin BME shell led to a marked increase in both the percentage of invaded cells, from 38.6 ± 10.5% to 57.6 ± 9.9% ($P < 0.0001$, $n \geq 16$), and the average invasion distance from 89.8 ± 26.9 μm to 147.3 ± 31 μm ($P < 0.0001$, $n \geq 16$), likely a result of the presence of laminin and collagen IV in the BME shell, which are known to facilitate cell attachment and increased metastatic potential (*22*). Increasing the BME shell thickness from 3.11 ± 0.35 μm to 4.45 ± 0.64 μm resulted in a decrease in the percentage of cells invaded from 57.6 ± 9.9% to 48 ± 15.8% ($P = 0.041$, $n = 20$), which is consistent with literature reports (*23*) that the BME layer serves as a physical barrier to breast cancer dissemination.

Qualitative analysis of CIMMS-generated images of invading cells provides additional insights that complement the quantitative results

(above). For example, the MDA-MB-231 cell line invades as individual cells into both simple (collagen 1) and core-shell (BME/collagen I) microgels (Fig. 3, D to F). But when exposed to a simple microgel composed only of BME, the cells exhibit a collective invasion morphology (*9*) and degrade the surface of the microgel in clusters (Fig. 3G). The E-cadherin expression pattern for invading cells is also interesting. For example, the number of E-cadherin–positive cells decreases with invasion distance and is different between microgel types (Fig. 3, H to J), suggesting a stromal-matrix effect on invasion. In particular, the leading invading cells (that penetrate furthest into the microgels) rarely express E-cadherin, a finding that is consistent with the well-known understanding that cells undergoing the endothelial-to-mesenchymal transition (EMT) are more invasive (*24*). This heterogeneity of E-cadherin expression (decreasing expression as a function of invasion difference) is markedly different than the case when the same cells are grown in conventional, 2D substrates with no invasion, which homogeneously express E-cadherin across the population (fig. S5).

In addition to MDA-MB-231 cells (Fig. 4A), CIMMS proved useful for evaluating the invasion behaviors of other breast cancer cell lines, including MDA-MB-468 and MCF-7 (Fig. 4, B to E). MDA-MB-468 cells did not consistently invade, instead extending invadopodia into the microgels (Fig. 4B); likewise, MCF-7 cells did not invade, instead forming 3D microclusters on the microgel surfaces (Fig. 4C). The lack of invasiveness observed for MDA-MB-468 and MCF-7 cells is consistent with results described previously (*25*), and in future work, it may be interesting to explore whether softer, more porous microgels (formed from low collagen I concentrations) are more attractive targets for invasion. Last, it has been reported (*26*) that *Arhgef18* and *BCAM* are up-regulated in circulating tumor cells (CTCs), and these genes have been shown to be strong indicators of metastasis with in vivo models. With this in mind, stable variants of the MDA-MB-468 cell line with up-regulation of these genes were evaluated, but the differences did not change the observed invasion phenotype (Fig. 4, D and E) relative to wild type (Fig. 4B), indicating that neither gene's overexpression is a driving condition of the invasion process.

CIMMS with transcriptomic analysis

A key feature of CIMMS is the capacity to access the contents of the devices, simply by removing the top plate to expose the cells and microgels within. As illustrated in fig. S6 (A to E), a custom method was developed to flash-freeze and dissect the microgels into thin sections, which are then digested to release the embedded cells for transcriptomic analysis. The sections formed by this technique occupy around 40 nl, a tiny volume relative to the 36-μl sections generated by dissecting microgels generated in microfluidic devices described previously (*27*). The higher precision reported here was found to be critical to enable separation of invading from noninvading populations of cells. To test this precision, a pseudoinvasion assay was devised with one cell type premixed into the hydrogel matrix (representing "invaded" cells) and a second cell type seeded at the edge of the microgels, as in conventional CIMMS assays (fig. S6F). Polymerase chain reaction (PCR) analysis of the invaded and "noninvaded" fractions confirms that the technique can distinguish the two cell types (fig. S6G). Note that unlike the rest of the procedures described herein, the process of microgel extraction and dissection is not automated. That is, the extraction/dissection process (described in detail in Methods) is straightforward but is manual; in the future, it should be possible to automate it using step motor–driven micromanipulators.

After establishing a reliable microgel sectioning technique, a series of CIMMS experiments was conducted to evaluate the transcriptomes of invading and noninvading cells. As an initial step, the data from all samples were evaluated broadly to determine overall analytical performance. First, a positive relationship exists between the number of reads and number of genes detected (fig. S7A), with no obvious trend related to sample origin, demonstrating a lack of bias in library depth and diversity relative to sample type (suggesting that major trends are driven by the gene expression content, rather than sequencing technicalities). Second, a broad underlying variance, which takes into consideration the gene content in the samples, was observed by reducing the data using Uniform Manifold Approximation and Projection (UMAP) (fig. S7B). Samples were not observed to cluster according to origin, suggesting that there were no marked differences between different subpopulations. This is expected, as the cells in the different subpopulations are from the same cell line; it was hypothesized that differences (if any) between the invaded and noninvaded subpopulations would be subtle. Last, Spearman correlation clustering analysis of invaded/noninvaded pairs and controls showed that cells grown in conventional 2D systems have a gene-level profile that differs substantially from those extracted from the microgel systems (fig. S7C). Furthermore, enhanced coverage for paired invading/noninvading samples was observed relative to cells extracted from "whole" microgels with no dissection, suggesting that analyzing the noninvading and invading cell samples separately provides more gene-level information than can be obtained by analyzing all of the cells together.

After establishing baseline performance for the RNA-seq data, attention was turned to evaluating differential gene expression between invading and noninvading cells. Statistical analysis revealed 244 genes that were significantly different [with false discovery rate

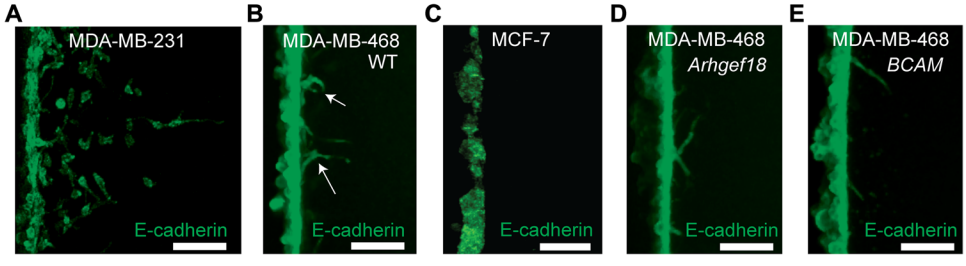

Fig. 4. Comparison of invasion morphologies for breast cancer cell lines by CIMMS. (**A** to **E**) Top-view fluorescent confocal microscope images of microgels for cells seeded at 400,000/ml on simple microgels [formed from collagen I (2.4 mg/ml)] and cultured to day 4, immunostained for E-cadherin (green). (A) MDA-MB-231 cells. (B) Wild-type (WT) MDA-MB-468 cells. Invadopodia indicated by white arrows. (C) MCF-7 cells. (D) MDA-MB-468 cells with stable overexpression of *Arhgef18*. (E) MDA-MB-468 cells with stable overexpression of *BCAM*. Scale bars, 100 μm (A to E).

(FDR) < 0.05; table S1, list 1] between invading (I avg.) and noninvading (N avg.) subpopulations (Fig. 5A). Pathways [WikiPathways 2019 (WP)] and gene ontology (GO) enriched in the list of differentially expressed genes were derived from EnrichR (*28*) and are listed in table S1 (list 2). As expected, top hits include ECM organization (GO:0030198, $P < 0.01$) and endopeptidase inhibitor activity (GO:0004866, $P < 0.01$), which suggests that the invading cells use endopeptidase to break down and remodel the ECM. The involvement of endopeptidases was validated by conducting CIMMS assays with (image-based readout) for MDA-MB-231cells incubated with the chemotherapeutic agent ilomastat (GM6001). As shown in fig. S8, exposure to the drug significantly reduces cell invasion distance ($P = 0.0004$) and the proportion of cells that invade ($P < 0.0001$). Other pathways found to correlate with invading cells include complement activation (WP545, $P < 0.01$) and cellular response to cytokine stimulus (GO:0071345, $P = 0.04$), suggesting that invading cells activate mechanisms related to immune surveillance. Last, similarities are noted between the genes found here to be differentially expressed for invasive versus noninvasive MDA-MB-231 cells and genes expressed in xenograft tumors generated from the same cell line (*29*). Together, these results suggest that up-regulation of only a small cohort of genes is necessary for MDA-MB-231 cells to invade, with key processes including breakdown of the ECM and the initiation of immune-related signaling pathways (perhaps in preparation for other steps of metastasis).

To analyze the differential gene expression further, four genes in the differentially expressed list identified by RNA-seq, formyl peptide receptor 1 (*FPR1*), B cell lymphoma 3–encoded protein (*BCL3*), fractalkine (*CX3CL1*), and E-cadherin (*CDH1*), were selected for further validation, on the basis of their well-known association with invasion in cancer cells. Specifically, FPR1 expression correlates with cancer cell invasion (*30*), BCL3 promotes metastasis and its overexpression confers survival advantage for breast tumors (*31*), CX3CL1 induces a diverse array of metastasis-related responses ranging from

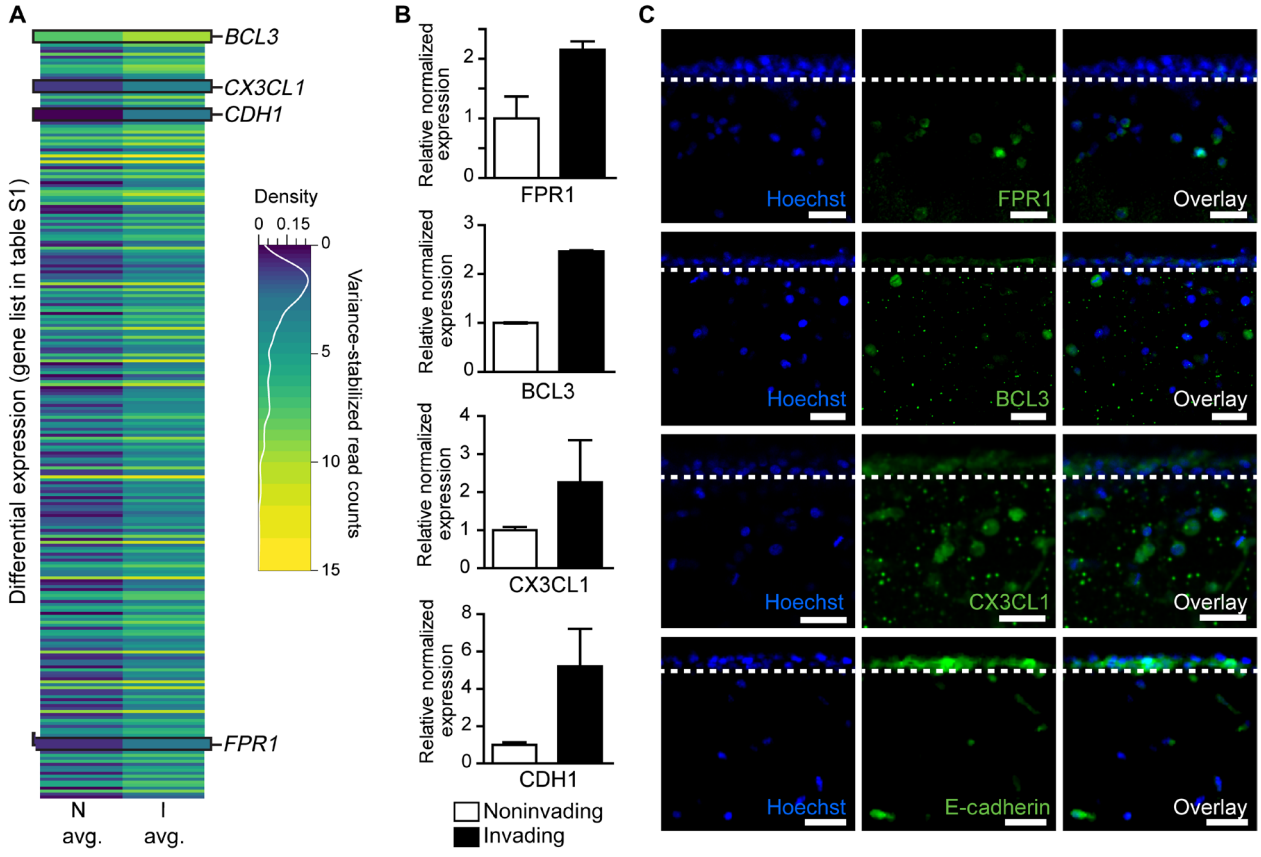

Fig. 5. Transcriptome analysis (and selected transcript and expression validation) of noninvaded versus invaded breast cancer cells in CIMMS. (**A**) Read counts were collected and averaged from invaded and noninvaded subpopulations of MDA-MB-231 cells harvested from five simple collagen I microgels (2.4 mg/ml) on day 4 after seeding at 400,000 cells/ml. The data are represented as a heat map of expression level (shown as variance-stabilized read counts per million, where yellow = high and blue = low) of the 244 genes (rows) determined to be significantly differentially expressed [with FDR < 0.05 based on the quasi-likelihood negative binomial generalized log-linear model (glmQLFit) from the edgeR package (*51*)] for noninvaded ("N avg.," left column) and invaded cells ("I avg.," right column). The white trace labeled "density" in the legend represents the distribution of the different expression levels in the dataset. Four genes (*FPR1*, *BCL3*, *CX3CL1*, and *CDH1*) are highlighted; the full list is found in table S1 (list 1). (**B**) ddPCR results for transcripts of *FPR1* (top), *BCL3* (mid-top), *CX3CL1* (mid-bottom), and *CDH1* (bottom) in noninvading (white bars) and invading (black bars) cells harvested from CIMMS experiments treated identically to (A), with error bars = 1 SD. Expression values for the four genes were normalized to the expression level of housekeeping gene glyceraldehyde phosphate dehydrogenase (*GAPDH*). (**C**) Top-view fluorescent confocal microscope images of microgels from CIMMS experiments treated identically to (A), with images in the left column stained blue for nuclei, images in the middle column immunostained green for FPR1 (top), BCL3 (mid-top), CX3CL1 (mid-bottom), and E-cadherin (bottom), and images in the right column overlaid. The white dashed lines indicate the edge of the gels. Scale bars, 50 μm.

increasing cell proliferation to immune surveillance (*32*), and E-cadherin down-regulation is a key marker of EMT (*24*). Each of these genes was found to have increased transcription in the invaded cells—this trend matches our expectations for FPR1, BCL3, and CX3CL1 but is (at first glance) counter to expectations for E-cadherin (*CDH1*). The same set of genes was subsequently evaluated by droplet-digital PCR (ddPCR) (Fig. 5B) and immunofluorescence staining (Fig. 5C). As shown, transcript and protein expression trends matched for FPR1, BCL3, and CX3CL1 but were opposite for E-cadherin. Discrepancies between mRNA and protein levels of E-cadherin have been reported in tumor samples previously (*33*), with a suggested mechanism of posttranscriptional regulation of E-cadherin (*CDH1*) mRNA in these cells. We propose that CIMMS will be a valuable tool to explore this phenomenon further in future studies.

Last, two pathway-level analyses were carried out to contextualize the results relative to what is known about cancer and invasion. First, the list of differentially expressed genes (invading versus noninvading) generated from CIMMS experiments was cross-referenced with the CancerSEA database (*34*), revealing strong correlations with previously published (*35*, *36*) RNA-seq results generated from CTCs collected from patients with breast cancer. As shown in Fig. 6A, genes correlating with invasion, DNA damage, and DNA repair were pathways in CTCs that were also associated with the invading subpopulation of MDA-MB-231 cells generated with CIMMS. Second, an unsupervised weighted gene correlation network analysis [WGCNA (*37*)] was used to partition the entire CIMMS–RNA-seq dataset into 40 gene-cluster modules (Fig. 6B). This analysis identified two modules significantly associated with the invading cell phenotype and one module significantly associated with the noninvading cell population ($P < 0.05$) (Fig. 6C). The two gene modules associated with the invading cells (enumerated in table S2, lists 1 and 2) contained genes such as *MGP* and *HYAL4*, which encode function in cell interactions with external matrices (*38*, *39*). These two modules also contained several of the same genes that were identified in the differential gene analysis (Fig. 5A and table S1, list 1), including *CX3CL1*, as well as genes associated with immune-mediated cell-cell interactions [e.g., *P2RY6* (*40*) and *KLRC1/3* (*41*)] and G protein transducers such as *CHRM3* (*42*). The module associated with noninvading cells (enumerated in table S2, list 3) was enriched for genes associated with type 2 diabetes mellitus, including WP1584 (Wikipathways human 2019, $P = 0.016$) and potassium ion binding (GO:0030955, $P = 0.045$) (*28*). Together, these results reveal a number of unique hits that have not been previously associated with cancer cell invasion, suggesting new players in pathways involving chemokines and cytokines that are translated via G protein–associated pathways and immune-related receptors.

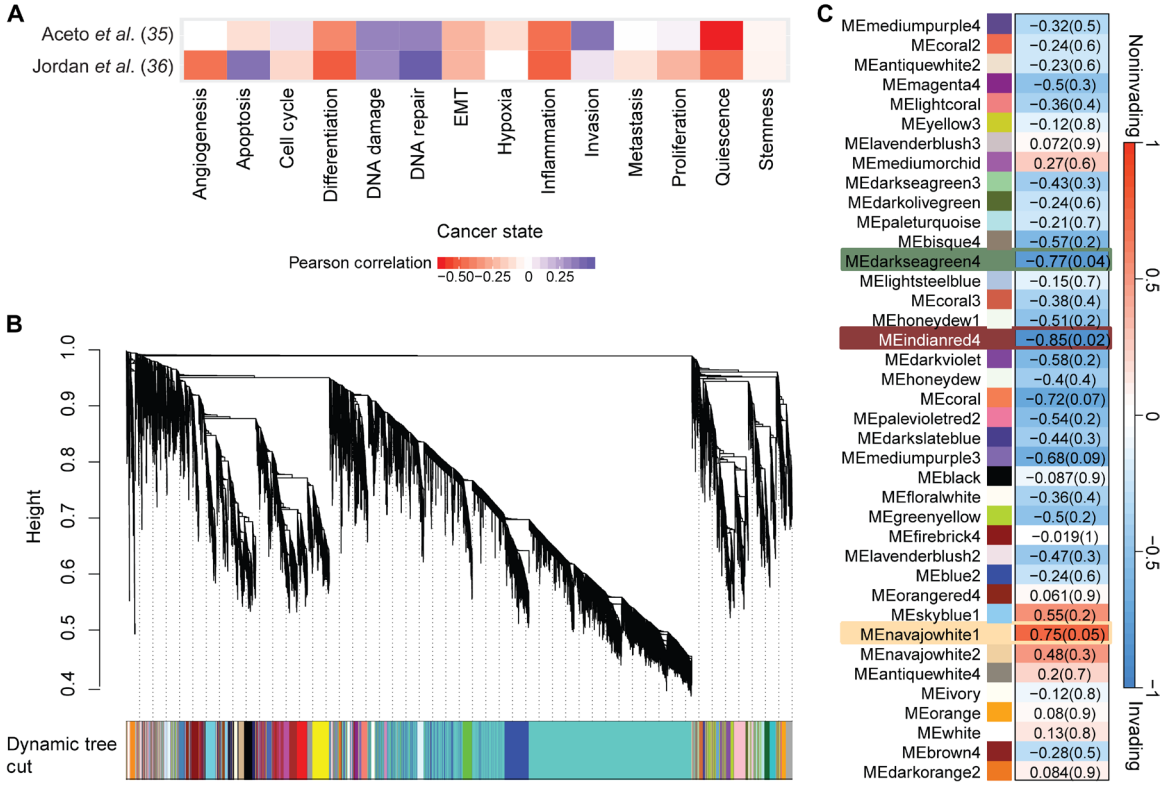

Fig. 6. Pathway-level CIMMS–RNA-seq observations of invasive versus noninvasive breast cancer cells. (**A**) Heat map of correlation (red, low; purple, high) between genes with elevated expression in invasive cells (from the CIMMS–RNA-seq dataset referenced in Fig. 5A and table S1, list 1) and functional states specific to cancer using CancerSEA (*34*) (columns), compared to existing breast cancer RNA-seq data from previous studies (*35*, *36*) (rows). (**B**) Dendrogram (top) of genes mapping to gene cluster modules (bottom) formed using the dynamic tree cut function from WGCNA (*37*) from the entire invasive versus noninvasive RNA-seq dataset. (**C**) Heat map illustrating the correlation between the gene modules from (B) and noninvading and invading cells (shown as a continuum from red = 1 for perfect correlation to noninvading to blue = −1 for perfect correlation to invading cells), with the *P* value for each state shown in parentheses. Gene lists corresponding to the two gene modules that are significantly ($P = 0.04$ and $P = 0.02$, respectively) associated with being invasive are found in table S2 (list 1; MEdarkseagreen4) and table S2 (list 2; MEindianred4); the gene list corresponding to the gene module significantly ($P = 0.05$) associated with being noninvasive are found in table S2 (list 3; MEnavajowhite1).

DISCUSSION

Microfluidics has allowed for the development of increasingly sophisticated cell culture and analysis tools that mimic aspects of the in vivo environment in a format that can be operated in vitro with a high degree of control. A topic of great interest in the microfluidics community has been cell invasion, and the methods that have been described previously can be categorized in terms of whether ECM remodeling is absent (type 1) (*3*–*6*) or present (type 2) (*11*–*16*). As demonstrated here, CIMMS is a member of the latter category that is capable of automating invasion and remodeling assays to generate quantitative and qualitative microscopy data in an open-source hardware format (*43*) that is accessible to any who wish to use it.

The microfluidic type 2 systems that have been described in the past decade have been led by pioneering examples from the Kamm group (*11*–*13*), at least one of which has recently become available as a commercial product. Like CIMMS, these methods rotate the axis of invasion (relative to well plate studies) to allow for high-resolution imaging in the *x*-*y* (horizontal) plane. A key selling point for the systems described by Kamm (*11*–*13*) and others (*14*–*16*) is their demonstrated capacity to analyze the effects of chemoattractant gradients and endothelial-cell barriers on invasion behavior. These capacities (chemoattractant gradients and inclusion of an endothelium layer) were not demonstrated here but represent attractive areas for exploration in the future. For example, in future CIMMS experiments, stromal cells secreting chemoattractant might be seeded onto one side of a microgel before the seeding of cancer cells on the opposing side, to generate a cell-mediated gradient for analysis.

The primary selling point for CIMMS is the capacity to combine a type 2 invasion assay with means to extract populations of cells with differential invasion profiles for transcriptome analysis, including RNA-seq. As described herein, the differential gene expression observed in invading versus noninvading cell populations showed that invading cells activate mechanisms to remodel the ECM-remodeling pathways, including endopeptidase inhibition. Other interesting findings include the identification of potential new players that correlate with (non)invasion in pathways involving chemokine/cytokine receptors and G protein transducers in breast cancer cell invasion (i.e., *P2RY6*, *KLRC1/3*, and *CHRM3*), as well as genes associated with invasion for matrix remodeling such as *MGP* and *HYAL4* (*38*, *39*).

CONCLUSIONS

Microfluidic platforms in which cells invade into hydrogel matrices have been developed to understand complex processes related to matrix remodeling; however, the systems described in the literature primarily report image-based analyses of cell invasion behavior. Here, we introduce CIMMS, a tool that makes it straightforward to isolate subpopulations of cells with different ECM-mediated invasiveness for RNA-seq. Key findings from this first study conducted with CIMMS include observation of up-regulation of known markers for invasion including BCL3, FPR1, and CX3CL1, and observation of up-regulation of chemokine/cytokine receptors and G protein transducers. We propose that the system described here will be useful for researchers who are asking new questions related to cell invasion and matrix remodeling, in all of their myriad forms.

METHODS

Reagents

Unless stated otherwise, general reagents were from Sigma-Aldrich (Oakville, ON), cell media reagents and Geltrex were from Thermo Fisher Scientific (Waltham, MA), and photolithography reagents were from Rohm and Haas (Marlborough, MA). Primary antibodies included collagen I (Sigma-Aldrich, catalog no. C2456), E-cadherin Alexa Fluor 488 (Cell Signaling Technology, Danvers, MA, catalog no. 3199), vimentin (Abcam, Cambridge, UK, catalog no. ab8978), FPR1 (Abcam, catalog no. ab113531), BCL3 (Abcam, catalog no. ab216877), CX3CL1 (Fisher Scientific, catalog no. 5013714), and collagen IV (Abcam, catalog no. ab6586). Secondary antibodies included anti-mouse immunoglobulin G (IgG) Alexa Fluor 647 (Cell Signaling Technology, catalog no. 4410), and anti-rabbit IgG Alexa Fluor 488 (Cell Signaling Technology, catalog no. 4412). Hoechst 33342 was purchased from Thermo Fisher Scientific (Waltham, MA). Predesigned ddPCR primers were purchased from Bio-Rad (Hercules, CA): CX3CL1 assay ID: dHsaEG5020779, BCL3 assay ID: dHSAEG5005131, CDH1 assay ID: dHsaEG5007039, FPR1 assay ID: dHsaEG5022504, and glyceraldehyde phosphate dehydrogenase (GAPDH) assay ID: dHsaEG5006642. Glass slides coated with chromium (100 nm) and AZ1500 photoresist (530 nm) were purchased from Telic Inc. (Santa Clarita, CA). Teflon AF 1600 was purchased from DuPont (Wilmington, DE). Parylene-C was obtained from Specialty Coating Systems (Indianapolis, IN). Bovine collagen I (3 mg/ml solution) was purchased from Advanced BioMatrix (San Diego, CA). Deionized (DI) water had a resistivity of >18 megohms·cm. All reagents manipulated on DMF were supplemented with 0.05% v/v F68 pluronics unless stated otherwise.

Device fabrication and operation

CIMMS devices were fabricated at the University of Toronto Nanofabrication Centre (TNFC). Bottom plates were fabricated in two stages. In the first stage (fig. S2C, bottom row, panel 1), Cr- and photoresist-coated glass substrates were patterned and etched using standard photolithography and metal etch techniques as described previously (*21*). The resulting substrates featured a 4 by 15 array of actuation electrodes (2.2 mm by 2.2 mm) adjacent to eight reservoir electrodes (16.4 mm by 6.7 mm) and eight dispensing electrodes (2.2 mm by 4.4 mm). After patterning, the substrates were immersed for 30 min in silanization solution: 1% (v/v) 3-(Trimethoxysilyl) propyl methacrylate (Specialty Coating Systems) in a 1:1 mixture of DI water:isopropanol (IPA). After silanization, the substrates were rinsed with IPA and baked at 80°C on a hot plate for 10 min. A first layer of parylene-C (~7 μm thick) was deposited via chemical vapor deposition (CVD) using an SCS 2010 Parylene Coater (Specialty Coating Systems), followed by spin-coating Teflon AF [1% (w/w) in fluorine FC-40, 2000 rpm, 30 s] and postbaking at 160°C on a hot plate for 10 min. A small number of bottom plates were used after the first stage (as in fig. S2, A and B), but most bottom plates were further processed in the second stage (fig. S2C, bottom row, panels 2 to 4) to form a linear array of superficial hydrophilic sites using a reactive-ion etching (RIE) method similar to one described previously (*44*) for other applications. Briefly, the substrates were coated with a second, sacrificial layer of parylene-C (~1 μm thick) by CVD and then a layer of S1811 photoresist by spin coating at 1000 rpm for 45 s. The photoresist was patterned to form a linear array of eight square exposed regions of parylene-C (each 1.5 mm by 1.5 mm, separated by 4.4 mm) centered between the two middle rows of the

actuation electrodes below. The substrates were then etched by RIE with O_2 plasma [150 mtorr, 100 W, 42-sccm (standard cubic centimeter per minute) O_2]. Etching time (approximately 6 min) was experimentally determined to etch through the second/sacrificial layer of parylene-C and the layer of Teflon AF and minimally into the first/dielectric layer of parylene-C. After RIE treatment, the sacrificial parylene-C layer was peeled off, leaving a surface that was mostly coated with hydrophobic Teflon AF, punctuated with a linear array of eight square hydrophilic sites (oxidized parylene-C).

CIMMS top plates (fig. S2C, top row) were formed from indium-tin-oxide–coated glass substrates (Delta Technologies, Loveland, CO) using methods similar to those used for the bottom plates. Briefly, substrates were coated with a first layer of parylene-C by CVD (~1 μm thick), a layer of Teflon AF by spin coating (~70-nm thick), a second, sacrificial layer of parylene-C by CVD (~1-μm thick), and a layer of photoresist by spin coating. The photolithography, RIE etching, and sacrificial layer peeling technique described above (for bottom plates) was applied, leaving a surface that was globally coated with Teflon AF, punctuated with a linear array of eight hydrophilic sites.

Before device assembly, top and bottom plates were sterilized with 70% ethanol, followed by air drying in a biosafety cabinet. Each top and bottom plate was then joined together with three layers of biocompatible double-sided tape (3M Company, Maplewood, MN) as spacers (~270 μm thick) while aligning pairs of analogous hydrophilic sites under a microscope. The volume of a unit droplet covering one driving electrode was ~1.3 μl. The volume of a droplet generated by passive dispensing on the hydrophilic sites was ~0.6 μl. Droplet manipulation was programmed and controlled via an open-source automation platform described elsewhere (*43*), used to apply sine wave potentials [85 to 100 V_{rms}, 10 kHz, conditions determined to be below the saturation forces (*45*) for the liquids used here] between bottom plate electrodes and the top-plate counter electrode.

Macroscale cell culture

All cells were maintained in Dulbecco's modified Eagle's medium completed with 10% fetal bovine serum, penicillin (100 U ml^{-1}), and streptomycin (100 μg ml^{-1}) and incubated in T-75 culture flasks in a humidified incubator with 5% CO_2 air environment at 37°C. Some MDA-MB-468 cells were stably transformed (*26*) to overexpress of BCAM or Arhgef18 and were provided by J. Lewis (University of Alberta). B16 and U87 cells were stably transformed to express tDTomato or enhanced green fluorescent protein (eGFP) (*46*), respectively, and were provided by W. Chan (University of Toronto). Before experiments, cells were trypsinized, washed in phosphate-buffered saline (PBS), and then suspended in complete medium at densities ranging from 50,000 to 600,000 cells/ml. In most cases, the media was untreated and cells were used immediately; in others, the media was supplemented with 25 μM ilomastat (GM6001) before being used for CIMMS experiments. Most suspensions were used for CIMMS or macroscale invasion assays (as below); in other experiments, aliquots (50,000 cells/ml, 0.2 to 1.0 ml) were dispensed into a six-well plate or eight-well chamber slides (Nalge Nunc, Rochester, NY) and cultured to day 2 before analysis by immunofluorescence and confocal imaging or RNA extraction (as below).

Cell invasion in digital microfluidic microgel systems

Each CIMMS assay began with microgel formation from sol-phase gel solutions, which were made fresh and kept on ice until use. Sol-phase collagen I (2.4 mg/ml) was generated by diluting the stock solution with 10× PBS, DI water, and 0.25 M NaOH in a 100:12.5:7.5:5 ratio (to form a pH 7 solution in 1× PBS); sol-phase collagen I (1.5 mg/ml) was diluted from 2.4 mg/ml solution in PBS. Sol-phase BME was formed by diluting stock Geltrex solution to 50, 25, or 10% in PBS.

To form simple microgels [from collagen I (2.4 or 1.5 mg/ml) or 50% BME], an appropriate solution was loaded into reservoirs on a DMF device, eight triple-unit droplets were dispensed onto the array of electrodes, and each was driven across a hydrophilic site, forming an array of passively dispensed subdroplets (Fig. 1D, panels 1 to 3). The residual droplets after passive dispensing were driven to waste reservoirs, and devices were placed in a culture flask with water reservoir to allow the microgels to thermally gel (37°C for 3 hours in cell culture incubator). To form core-shell microgels, sol-phase BME (10 or 25%) was loaded into reservoirs; eight triple-unit droplets were dispensed onto the array of electrodes and then passed across simple microgels at approximately 2 mm/s (Fig. 1D, panels 4 to 6), with residual droplets driven to waste reservoirs. This results in the formation of thin encapsulating layers containing BME, which were found to gel upon incubation at 37°C for 1 hour. Shell thicknesses were determined by confocal microscopy with immunofluorescent staining (see below).

Cell invasion experiments were initiated by loading cell suspensions into reservoirs and dispensing eight single-unit droplets onto the array, which were driven such that each droplet touched one side of a microgel (Fig. 1F, panels 1 to 3). The device was then tilted 90° and incubated overnight, after which the devices were returned to normal orientation. Devices were stored in a culture flask with water reservoir in the cell culture incubator when not in use, and cells were evaluated by immunofluorescence or ddPCR/RNA-seq on day 2 or 4 of culture, as described below. For cells cultured to day 4, on day 2, fresh, complete media (untreated in most cases, supplemented with 25 μM ilomastat in some cases) was loaded into a reservoir, and eight double-unit droplets were dispensed onto the electrode array and merged with each droplet containing cells (adjacent to microgels).

Macroscale invasion assays

Aliquots (0.25 ml) of sol-phase collagen I (2.4 mg/ml formed as above) were deposited into eight-well chamber slides (Nalge Nunc), and thermally gelled (37°C for 3 hours). Aliquots (200 μl) of MDA-MB-231 cell suspension (50,000 cells/ml) were seeded onto the collagen I surfaces and allowed to settle and adhere for 2 hours before 200 μl of fresh, complete media was added to each well. Fresh complete media was supplemented on day 2, and cells were allowed to invade in the humidified incubator to day 4. Most gels were evaluated by immunofluorescent staining and microscopy (below); some were evaluated by cryosectioning and staining. In the latter case, gels were gently washed with PBS and then fixed in paraformaldehyde (0.4 ml of 4% solution per gel for 10 min). Gels were washed three times with PBS and then covered with tissue embedding medium [optimum cutting temperature (OCT) compound, VWR] and flash-frozen by immersing the chambers in liquid nitrogen for ~1 min. Each gel was then removed from its chamber, flipped 90°, and positioned in a cryosection mold prefilled with OCT compound. The filled cryosection molds were frozen by immersing in liquid nitrogen and then stored at −80°C until analysis. Samples were processed by Pathology Research Program Laboratory at the University Healthy Network (PRP). Sections with thicknesses

of 10 μm were generated and stained with hematoxylin and eosin by standard techniques.

Immunofluorescent staining and imaging

In CIMMS experiments, immunofluorescent staining was performed in situ in an automated 15-step procedure, in which each step comprised loading a reagent into one or more reservoirs, dispensing eight triple-unit droplets onto the actuation array, driving each droplet onto a microgel, incubating at a particular temperature, and then driving the droplets to a waste reservoir (which were periodically emptied by applications of a Kimwipe). The procedure is indicated below as "Step X: reagent, incubation period, temperature" (where RT means room temperature). Step 1 (wash): PBS with 0.05% (v/v) F68, 0 min, RT. Step 2 (fix): 4% paraformaldehyde with 0.05% (v/v) F68, 10 min, RT. Step 3 (wash): PBS with 0.05% (v/v) Brij 35, 0 min, RT. Step 4 (permeabilize): 0.2% Tween 20 (v/v) PBS, 15 min, RT. Step 5 (wash): repeat of step 3. Step 6 (block): 10% skim milk powder (w/v) in PBS with 0.05% Brij 35, 2 hours, RT. Step 7 (primary): primary antibody solution diluted 1:100 in the blocking solution from step 6, overnight, 4°C. Step 8 (wash): PBS with 0.05% (v/v) Brij 35, 10 min, RT. Steps 9 and 10 (washes): repeats of step 8. [In experiments not requiring secondary antibodies (e.g., for primary E-cadherin antibodies conjugated to dye), steps 11 to 14 were skipped.] Step 11 (secondary): secondary antibody solution diluted 1:100 in the blocking solution from step 6, 2 hours, RT. Steps 12 to 14 (washes): repeats of step 8. Step 15 (Hoechst): Hoechst solution diluted 1:10,000 in PBS with 0.05% (v/v) Brij 35, 20 min, RT. Macroscale systems in well plates (3D gel invasion experiments and 2D cell culture experiments) were stained in the same 15-step procedure used for CIMMS, except that all reagent aliquoting and aspiration steps were manually performed by pipette, and the reagent volumes were 0.4 ml for step 2 and 0.2 ml for steps 1 and 3 to 15.

After staining, gels and other samples were imaged with the Nikon A1 confocal microscope at the University of Toronto Centre for Microfluidics Systems (CMS). For 3D analysis, images were collected at 2.55-μm intervals along the *z* axis. For microgels, a custom script was developed and run in Imaris image analysis software to quantify invasion distances of cells with different stains. Briefly, the script removes seven confocal z slices from top and bottom layers (adjacent to the device top and bottom plates) as in fig. S4D. The nuclear coordinates of all cells in the remaining images (fig. S4E) are enumerated, and the coordinates of the seeded surface are determined by the large number of noninvaded cells. The cell corresponding to each nucleus that is ≥16.5 μm past the seeded surface is designated invaded. The distance of each invaded cell's nucleus from the seeded surface is recorded, and the ratio of the number of invaded cells relative to the total number of cells is expressed as a percentage. Last, cells are identified as E-cadherin positive when the intensity of the appropriate color channel is ≥5% of the maximum intensity.

SEM imaging

A routine method for fixing, dehydrating, and drying samples for analysis by SEM was adapted to be automated in a 12-step procedure by DMF. Each step comprised loading a reagent into one or more reservoirs, dispensing one or more triple-unit droplets onto the actuation array, driving each droplet onto a microgel, incubating at a particular temperature, and then driving the droplets to a waste reservoir (which were periodically emptied by applications of a Kimwipe). The procedure is indicated below as "Step X: reagent, incubation period, temperature". Step 1 (fix): 4% glutaraldehyde with 0.05% (v/v) F68, 2.5 hours, RT. Step 2 (dehydrate): 35% ethanol in water with 0.05% (v/v) F68, 30 min, RT. Steps 3 to 9 (dehydrate): repeat step 2 with 70, 80, 90, 95, 100, 100, and 100% ethanol. Step 10 (dry): 50% hexamethyldisilazane (HMDS) in water, 30 min, RT. Steps 11 and 12 (dry): repeat of step 10 with 100% HMDS. The device with dry microgels was left in a fume hood for 12 hours at RT. The device was disassembled and the top plate with attached microgels was left in a fume hood to dry for 24 hours at RT. The samples were then mounted on aluminum stubs, sputter-coated with a layer of gold using a Polaron SC7640 sputter coater (Quorum Technologies, UK) and imaged using a Hitachi S-3400 variable pressure scanning electron microscope (Microscopy Imaging Laboratory, University of Toronto) operating at 5 kV.

Transcriptome extraction and measurement

Microgels bearing invaded cells at the completion of a CIMMS assay (or a pseudoinvasion assay, as described below) were sectioned using a custom dissection technique (fig. S6) before transcriptomic analysis. Briefly, the media droplets adjacent to the microgels were wicked away by applying a Kimwipe, and the device was flash-frozen by placing it on a metal plate chilled with dry ice. Then, the top and bottom plates were carefully separated, and the plate not bearing the microgels was removed. The chilled metal plate (bearing the plate with microgels) was mounted on a dissection microscope. A replaceable no. 15 sterile scalpel blade (Almedic, Concord, ON) attached to a magnetic arm fixed to a three-axis micromanipulator (PT3A, Thorlabs) was carefully maneuvered into place under the microscope such that the blade hovered above the location of dissection. With a gentle push down, a single slice of the microgel was dissected (with the thin dimension of the slice in the invasion dimension). This process was repeated until five or more slices were formed (replacing the blade after each slice) from each microgel. Slice thicknesses were measured to be 93.7 ± 15.2 μm (n = 5). The slices naturally adhere to the scalpels; thus, after each excision, each scalpel-and-slice was removed and placed on dry ice for further processing. The first slice excised from each microgel was designated to contain the noninvaded cell fraction. The remaining slices were further trimmed (to remove ~100 μm on each edge not in the invasion axis) and were pooled and designated as the "invaded" cell fraction.

Most experiments were designed to test for differences between invaded and noninvaded cell fractions for MDA-MB-231 cells harvested from CIMMS devices on day 4 after seeding at 400,000 cells/ml in simple collagen I gels (2.4 mg/ml). Controls were also evaluated, including whole-gel samples in identical experiments but with no dissections (with invaded and noninvaded cells kept together) and 2D cell culture samples in which MDA-MB-231 were grown on well plates for the same durations as CIMMS experiments (reaching 70% confluence) before analysis. (In place of dissection, in the 2D control, cells were scraped from the well by a cell scraper, centrifuged, and resuspended in PBS.) In other experiments, "pseudoinvasion" assays were performed. Briefly, pseudoinvasion assays followed standard CIMMS procedure (described above) to form simple collagen I microgels (2.4 mg/ml), which were seeded with U87-eGFP cells (at the edge of each microgel) at 100,000 cells/ml. The key difference relative to CIMMS assays: the sol-form gel solution was supplemented with B16-tDTomato cells at 25,000 cells/ml (representing "invaded" cells) before microgel formation. On day 1 after seeding, microgels were dissected as described above.

Scalpels bearing adhered microgel slices (or intact microgels) were submersed in 350 µl of lysis buffer from a Norgen Biotek Single cell RNA isolation kit (Thorold, ON) and incubated at 42°C for 30 min, vortexing for 15 s every 10 min, and then processed according to the manufacturer's instructions. The RNA extracted from all microgels (up to eight) originating from the same state (i.e., invaded, "pseudo-invaded," or noninvaded) was then combined into a single sample and amplified following the manufacturer's instructions for the Takara Bio SMART-Seq v4 Ultra Low Input RNA Kit for Sequencing (Kusatsu, Japan). Amplified complementary DNA (cDNA) was then purified using Agencourt AMPure XP beads (Brea, CA) following the manufacturer's instructions. The concentration of cDNA generated in this final step was determined using the Qubit 1X dsDNA HS (High-Sensitivity) Assay Kit (Thermo Fisher Scientific) on a Qubit Fluorometer (Thermo Fisher Scientific). 2D control cells were treated identically as above (including extraction, amplification, and purification), except with a substitution of the PureLink RNA Mini Kit (Thermo Fisher Scientific, following the manufacturer's instructions) for the Norgen Biotek kit for the first step.

Processed cDNA samples (prepared as above) were analyzed by (i) RNA-seq (CIMMS assays), (ii) ddPCR (CIMMS assays), or (iii) conventional PCR (pseudoinvasion assays). Briefly, for (i), samples were diluted and processed for library preparation with Nextera XT kits (Illumina, San Diego, CA) per manufacturing protocol and purified again with AMPure XP beads (as above), before being quality-checked with an Agilent 2100 Bioanalyzer. All samples had average base pair (bp) length between 500 and 700 and a mean concentration of 16.9 ng/µl. Samples were sequenced on a NextSeq500 (Illumina) at the Donnelly Sequencing Centre (Toronto, ON), to generate paired-end, high-throughput reads averaging at 12.5 million reads per sample (2 × 75–bp read length, V2 chemistry). Data generated were processed as described below. For (ii), samples were processed according to the manufacturer's instructions for the QX200 ddPCR EvaGreen Supermix (Bio-Rad) using PrimePCR ddPCR Expression EvaGreen predesigned primers (Bio-Rad, listed in the reagents section) and then evaluated via the QX200 Droplet Generator (Bio-Rad) and thermocycled per the recommended setting from the Supermix protocol. Last, reaction products were analyzed on the QX200 Droplet Reader (Bio-Rad) to determine expression levels, which were then normalized to the expression of GAPDH. For (iii), samples were processed with Taq DNA Polymerase kits (Thermo Fisher Scientific) according to the manufacturer's instructions. The reactions were then thermocycled at the recommended settings for the kit (i.e., annealing temperature 55°C), and gel electrophoresis was performed on the products using a 2% (w/v) agarose gel and visualized using the Gel Doc EZ Imaging System (Bio-Rad).

RNA-seq analysis

Raw Fastq files originating from RNA-seq analysis were trimmed with Trimmomatic (*47*) with a sliding window size of 5 and a phred33 score of 20. These reads were then mapped with STAR aligner (2.7) (*48*) to the human genome, version GRCh38. Read counts were extracted using Featurecounts (*49*). In preliminary screens, RNA-seq datasets exhibiting multimodal read distributions were removed. UMAP was used for dimensionality reduction and ggplot2 for visualization of the results (*50*). Statistical analysis for differential gene expression was implemented using the quasi-likelihood negative binomial generalized log-linear model (glmQLFit) from edgeR (*51*). Genes with an FDR value below 0.05 were considered significant and hierarchically clustered and visualized with a heat map plotted using ggplot2 (*52*). CancerSEA was used to correlate differentially expressed genes to functional states of cancer cells by comparing to databases from literature reports, and gene lists were inputted into the database to generate correlation tables. Weighted Gene Correlation (WGCNA) was used to fill out pathways of differentially expressed genes, taking into account "hub" genes and using a correlation-based approach to pathways associated with either invasive or noninvasive cells (*37*). All scripts used in this analysis are available at http://microfluidics.utoronto.ca/gitlab/cimms/CIMMS_BreastCancerInvasion.

SUPPLEMENTARY MATERIALS

Supplementary material for this article is available at http://advances.sciencemag.org/cgi/content/full/6/29/eaba9589/DC1

View/request a protocol for this paper from *Bio-protocol*.

REFERENCES AND NOTES

1. O. Veiseh, F. M. Kievit, R. G. Ellenbogen, M. Zhang, Cancer cell invasion: Treatment and monitoring opportunities in nanomedicine. *Adv. Drug Deliv. Rev.* **63**, 582–596 (2011).
2. A. Albini, Y. Iwamoto, H. K. Kleinman, G. R. Martin, S. A. Aaronson, J. M. Kozlowski, R. N. McEwan, A rapid in vitro assay for quantitating the invasive potential of tumor cells. *Cancer Res.* **47**, 3239–3245 (1987).
3. Y.-C. Chen, S. G. Allen, P. N. Ingram, R. Buckanovich, S. D. Merajver, E. Yoon, Single-cell migration chip for chemotaxis-based microfluidic selection of heterogeneous cell populations. *Sci. Rep.* **5**, 9980 (2015).
4. C. L. Yankaskas, K. N. Thompson, C. D. Paul, M. I. Vitolo, P. Mistriotis, A. Mahendra, V. K. Bajpai, D. J. Shea, K. M. Manto, A. C. Chai, N. Varadarajan, A. Kontrogianni-Konstantopoulos, S. S. Martin, K. Konstantopoulos, A microfluidic assay for the quantification of the metastatic propensity of breast cancer specimens. *Nat. Biomed. Eng.* **3**, 452–465 (2019).
5. M. Poudineh, M. Labib, S. Ahmed, L. N. M. Nguyen, L. Kermanshah, R. M. Mohamadi, E. H. Sargent, S. O. Kelley, Profiling functional and biochemical phenotypes of circulating tumor cells using a two-dimensional sorting device. *Angew. Chem. Int. Ed. Engl.* **56**, 163–168 (2017).
6. S. P. Desai, S. N. Bhatia, M. Toner, D. Irimia, Mitochondrial localization and the persistent migration of epithelial cancer cells. *Biophys. J.* **104**, 2077–2088 (2013).
7. R. A. Mosig, L. Lin, E. Senturk, H. Shah, F. Huang, P. Schlosshauer, S. Cohen, R. Fruscio, S. Marchini, M. D'Incalci, R. Sachidanandam, P. Dottino, J. A. Martignetti, Application of RNA-seq transcriptome analysis: CD151 is an invasion/migration target in all stages of epithelial ovarian cancer. *J. Ovarian Res.* **5**, 4 (2012).
8. P. Friedl, S. Alexander, Cancer invasion and the microenvironment: Plasticity and reciprocity. *Cell* **147**, 992–1009 (2011).
9. A. G. Clark, D. M. Vignjevic, Modes of cancer cell invasion and the role of the microenvironment. *Curr. Opin. Cell Biol.* **36**, 13–22 (2015).
10. V. Brekhman, G. Neufeld, A novel asymmetric 3D in-vitro assay for the study of tumor cell invasion. *BMC Cancer* **9**, 415 (2009).
11. I. K. Zervantonakis, S. K. Hughes-Alford, J. L. Charest, J. S. Condeelis, F. B. Gertler, R. D. Kamm, Three-dimensional microfluidic model for tumor cell intravasation and endothelial barrier function. *Proc. Natl. Acad. Sci. U.S.A.* **109**, 13515–13520 (2012).
12. J. S. Jeon, S. Bersini, M. Gilardi, G. Dubini, J. L. Charest, M. Moretti, R. D. Kamm, Human 3D vascularized organotypic microfluidic assays to study breast cancer cell extravasation. *Proc. Natl. Acad. Sci. U.S.A.* **112**, 214–219 (2015).
13. D. Truong, J. Puleo, A. Llave, G. Mouneimne, R. D. Kamm, M. Nikkhah, Breast cancer cell invasion into a three dimensional tumor-stroma microenvironment. *Sci. Rep.* **6**, 34094 (2016).
14. Y.-C. Toh, A. Raja, H. Yu, D. van Noort, Y.-C. Toh, A. Raja, H. Yu, D. Van Noort, A 3D microfluidic model to recapitulate cancer cell migration and invasion. *Bioengineering* **5**, 29 (2018).
15. C. Frick, P. Dettinger, J. Renkawitz, A. Jauch, C. T. Berger, M. Recher, T. Schroeder, M. Mehling, Nano-scale microfluidics to study 3D chemotaxis at the single cell level. *PLOS ONE* **13**, e0198330 (2018).
16. W. Han, S. Chen, W. Yuan, Q. Fan, J. Tian, X. Wang, L. Chen, X. Zhang, W. Wei, R. Liu, J. Qu, Y. Jiao, R. H. Austin, L. Liu, Oriented collagen fibers direct tumor cell intravasation. *Proc. Natl. Acad. Sci. U.S.A.* **113**, 11208–11213 (2016).
17. I. A. Eydelnant, B. B. Li, A. R. Wheeler, Microgels on-demand. *Nat. Commun.* **5**, 3355 (2014).
18. M.-Y. Chiang, Y.-W. Hsu, H.-Y. Hsieh, S.-Y. Chen, S.-K. Fan, Constructing 3D heterogeneous hydrogels from electrically manipulated prepolymer droplets and crosslinked microgels. *Sci. Adv.* **2**, e1600964 (2016).

19. B. F. Bender, A. P. Aijian, R. L. Garrell, Digital microfluidics for spheroid-based invasion assays. *Lab Chip* **16**, 1505–1513 (2016).
20. B. A. Nestor, E. Samiei, R. Samanipour, A. Gupta, A. Van den Berg, M. Diaz de Leon Derby, Z. Wang, H. R. Nejad, K. Kim, M. Hoorfar, Digital microfluidic platform for dielectrophoretic patterning of cells encapsulated in hydrogel droplets. *RSC Adv.* **6**, 57409–57416 (2016).
21. I. A. Eydelnant, U. Uddayasankar, B. Li, M. W. Liao, A. R. Wheeler, Virtual microwells for digital microfluidic reagent dispensing and cell culture. *Lab Chip* **12**, 750–757 (2012).
22. R. Fridman, G. Giaccone, T. Kanemoto, G. R. Martin, A. F. Gazdar, J. L. Mulshine, Reconstituted basement membrane (matrigel) and laminin can enhance the tumorigenicity and the drug resistance of small cell lung cancer cell lines. *Proc. Natl. Acad. Sci.* **87**, 6698–6702 (1990).
23. L. C. Kelley, L. L. Lohmer, E. J. Hagedorn, D. R. Sherwood, Traversing the basement membrane in vivo: A diversity of strategies. *J. Cell Biol.* **204**, 291–302 (2014).
24. I. Y. Wong, S. Javaid, E. A. Wong, S. Perk, D. A. Haber, M. Toner, D. Irimia, Collective and individual migration following the epithelial–mesenchymal transition. *Nat. Mater.* **13**, 1063–1071 (2014).
25. P. A. Kenny, G. Y. Lee, C. A. Myers, R. M. Neve, J. R. Semeiks, P. T. Spellman, K. Lorenz, E. H. Lee, M. H. Barcellos-Hoff, O. W. Petersen, J. W. Gray, M. J. Bissell, The morphologies of breast cancer cell lines in three-dimensional assays correlate with their profiles of gene expression. *Mol. Oncol.* **1**, 84–96 (2007).
26. N. Kanwar, P. Hu, P. Bedard, M. Clemons, D. McCready, S. J. Done, Identification of genomic signatures in circulating tumor cells from breast cancer. *Int. J. Cancer* **137**, 332–344 (2015).
27. B. P. Mahadik, T. D. Wheeler, L. J. Skertich, P. J. A. Kenis, B. A. C. Harley, Microfluidic generation of gradient hydrogels to modulate hematopoietic stem cell culture environment. *Adv. Healthc. Mater.* **3**, 449–458 (2014).
28. M. V. Kuleshov, M. R. Jones, A. D. Rouillard, N. F. Fernandez, Q. Duan, Z. Wang, S. Koplev, S. L. Jenkins, K. M. Jagodnik, A. Lachmann, M. G. McDermott, C. D. Monteiro, G. W. Gundersen, A. Ma'ayan, Enrichr: A comprehensive gene set enrichment analysis web server 2016 update. *Nucleic Acids Res.* **44**, W90–W97 (2016).
29. A. J. Minn, G. P. Gupta, P. M. Siegel, P. D. Bos, W. Shu, D. D. Giri, A. Viale, A. B. Olshen, W. L. Gerald, J. Massagué, Genes that mediate breast cancer metastasis to lung. *Nature* **436**, 518–524 (2005).
30. S.-Q. Li, N. Su, P. Gong, H.-B. Zhang, J. Liu, D. Wang, Y.-P. Sun, Y. Zhang, F. Qian, B. Zhao, Y. Yu, R. D. Ye, The expression of formyl peptide receptor 1 is correlated with tumor invasion of human colorectal cancer. *Sci. Rep.* **7**, 5918 (2017).
31. X. Chen, X. Cao, X. Sun, R. Lei, P. Chen, Y. Zhao, Y. Jiang, J. Yin, R. Chen, D. Ye, Q. Wang, Z. Liu, S. Liu, C. Cheng, J. Mao, Y. Hou, M. Wang, U. Siebenlist, Y. Eugene Chin, Y. Wang, L. Cao, G. Hu, X. Zhang, Bcl-3 regulates TGFβ signaling by stabilizing Smad3 during breast cancer pulmonary metastasis. *Cell Death Dis.* **7**, e2508 (2016).
32. J. Y. S. Tsang, Y.-B. Ni, S.-K. Chan, M.-M. Shao, Y.-K. Kwok, K.-W. Chan, P. H. Tan, G. M. Tse, CX3CL1 expression is associated with poor outcome in breast cancer patients. *Breast Cancer Res. Treat.* **140**, 495–504 (2013).
33. S. B. Sonne, C. E. Hoei-Hansen, J. E. Nielsen, A. S. Herlihy, A. M. Andersson, K. Almstrup, G. Daugaard, N. E. Skakkebaek, H. Leffers, E. Rajpert-De Meyts, CDH1 (E-cadherin) in testicular germ cell neoplasia: Suppressed translation of mRNA in pre-invasive carcinoma in situ but increased protein levels in advanced tumours. *APMIS* **114**, 549–558 (2006).
34. H. Yuan, M. Yan, G. Zhang, W. Liu, C. Deng, G. Liao, L. Xu, T. Luo, H. Yan, Z. Long, A. Shi, T. Zhao, Y. Xiao, X. Li, CancerSEA: A cancer single-cell state atlas. *Nucleic Acids Res.* **47**, D900–D908 (2019).
35. N. Aceto, A. Bardia, B. S. Wittner, M. C. Donaldson, R. O'Keefe, A. Engstrom, F. Bersani, Y. Zheng, V. Comaills, K. Niederhoffer, H. Zhu, O. Mackenzie, T. Shioda, D. Sgroi, R. Kapur, D. T. Ting, B. Moy, S. Ramaswamy, M. Toner, D. A. Haber, S. Maheswaran, AR expression in breast cancer CTCs associates with bone metastases. *Mol. Cancer Res.* **16**, 720–727 (2018).
36. N. V. Jordan, A. Bardia, B. S. Wittner, C. Benes, M. Ligorio, Y. Zheng, M. Yu, T. K. Sundaresan, J. A. Licausi, R. Desai, R. M. O'Keefe, R. Y. Ebright, M. Boukhali, S. Sil, M. L. Onozato, A. J. Iafrate, R. Kapur, D. Sgroi, D. T. Ting, M. Toner, S. Ramaswamy, W. Haas, S. Maheswaran, D. A. Haber, HER2 expression identifies dynamic functional states within circulating breast cancer cells. *Nature* **537**, 102–106 (2016).
37. P. Langfelder, S. Horvath, WGCNA: An R package for weighted correlation network analysis. *BMC Bioinformatics* **9**, 559 (2008).
38. L. Cancela, C. L. Hsieh, U. Francke, P. A. Price, Molecular structure, chromosome assignment, and promoter organization of the human matrix Gla protein gene. *J. Biol. Chem.* **265**, 15040–15048 (1990).
39. A. B. Csoka, G. I. Frost, R. Stern, The six hyaluronidase-like genes in the human and mouse genomes. *Matrix Biol.* **20**, 499–508 (2001).
40. J. Lattin, D. A. Zidar, K. Schroder, S. Kellie, D. A. Hume, M. J. Sweet, G-protein-coupled receptor expression, function, and signaling in macrophages. *J. Leukoc. Biol.* **82**, 16–32 (2007).
41. B. Plougastel, T. Jones, J. Trowsdale, Genomic structure, chromosome location, and alternative splicing of the human NKG2A gene. *Immunogenetics* **44**, 286–291 (1996).
42. S. Patowary, E. Alvarez-Curto, T.-R. Xu, J. D. Holz, J. A. Oliver, G. Milligan, V. Raicu, The muscarinic M_3 acetylcholine receptor exists as two differently sized complexes at the plasma membrane. *Biochem. J.* **452**, 303–312 (2013).
43. R. Fobel, C. Fobel, A. R. Wheeler, DropBot: An open-source digital microfluidic control system with precise control of electrostatic driving force and instantaneous drop velocity measurement. *Appl. Phys. Lett.* **102**, 193513 (2013).
44. D. Witters, N. Vergauwe, S. Vermeir, F. Ceyssens, S. Liekens, R. Puers, J. Lammertyn, Biofunctionalization of electrowetting-on-dielectric digital microfluidic chips for miniaturized cell-based applications. *Lab Chip* **11**, 2790–2794 (2011).
45. I. Swyer, R. Fobel, A. R. Wheeler, Velocity saturation in digital microfluidics. *Langmuir* **35**, 5342–5352 (2019).
46. Y. Y. Chen, P. N. Silva, A. M. Syed, S. Sindhwani, J. V. Rocheleau, W. C. W. Chan, Clarifying intact 3D tissues on a microfluidic chip for high-throughput structural analysis. *Proc. Natl. Acad. Sci. U.S.A.* **113**, 14915–14920 (2016).
47. A. M. Bolger, M. Lohse, B. Usadel, Trimmomatic: A flexible trimmer for Illumina sequence data. *Bioinformatics* **30**, 2114–2120 (2014).
48. A. Dobin, C. A. Davis, F. Schlesinger, J. Drenkow, C. Zaleski, S. Jha, P. Batut, M. Chaisson, T. R. Gingeras, STAR: Ultrafast universal RNA-seq aligner. *Bioinformatics* **29**, 15–21 (2013).
49. Y. Liao, G. K. Smyth, W. Shi, featureCounts: An efficient general purpose program for assigning sequence reads to genomic features. *Bioinformatics* **30**, 923–930 (2014).
50. L. McInnes, J. Healy, N. Saul, L. Großberger, UMAP: Uniform manifold approximation and projection. *J. Open Source Softw.* **3**, 861 (2018).
51. M. D. Robinson, D. J. McCarthy, G. K. Smyth, edgeR: A bioconductor package for differential expression analysis of digital gene expression data. *Bioinformatics* **26**, 139–140 (2010).
52. V. Gómez-Rubio, ggplot2 - elegant graphics for data analysis (2nd edition). *J. Stat. Softw.* **77**, 10.18637/jss.v077.b02, (2017).
53. R. L. Blackmon, R. Sandhu, B. S. Chapman, P. Casbas-Hernandez, J. B. Tracy, M. A. Troester, A. L. Oldenburg, Imaging extracellular matrix remodeling in vitro by diffusion-sensitive optical coherence tomography. *Biophys. J.* **110**, 1858–1868 (2016).
54. N. R. Lang, K. Skodzek, S. Hurst, A. Mainka, J. Steinwachs, J. Schneider, K. E. Aifantis, B. Fabry, Biphasic response of cell invasion to matrix stiffness in three-dimensional biopolymer networks. *Acta Biomater.* **13**, 61–67 (2015).

Acknowledgments: We thank J. Lewis (University of Alberta) and W. Chan (University of Toronto) for providing transformed cells. We thank R. Kamm (MIT), A. McGuigan (University of Toronto), and N. Kanwar (Hospital for Sick Children) for advice and discussions. We thank the Donnelly Sequencing Centre for assistance with sequencing and Y. Zhou and E. H. Xu (University of Toronto Nanofabrication Centre) for support on cleanroom fabrication. **Funding:** This research is supported by the Natural Sciences and Engineering Research Council of Canada (NSERC) (grants RGPIN 2014-06042 and CREATE 482073-16), the Canada Foundation for Innovation (CFI) (#36661, with matching funds from the Province of Ontario), and by the University of Toronto's Medicine by Design initiative, which receives funding from the Canada First Research Excellence Fund (CFREF). Finally, B.B.L. thanks NSERC for a graduate fellowship and A.R.W. thanks the Canada Research Chair (CRC) program for a CRC. **Author contributions:** B.B.L., M.D.C., and A.R.W. conceived the concept of invasion assay on DMF. B.B.L. fabricated devices, performed invasion experiments, analyzed most of the invasion data, and collected and prepared samples for transcriptomic analysis. E.Y.S. and B.B.L. carried out the RNA-seq study, and E.Y.S. performed bioinformatics analysis. M.D.C. advised on experiments and provided troubleshooting advice. S.Z. and B.B.L. constructed the microgel dissection station, and B.B.L. developed the microgel dissection method. B.T.V.D. wrote the script to quantify invasion distance and analyzed invasion data. S.J.D. provided materials and advised on experiments. B.B.L., E.Y.S., and A.R.W. wrote and edited the manuscript. All authors discussed and commented on the manuscript. **Competing interests:** The authors declare that they have no competing interests. **Data and materials availability:** All data needed to evaluate the conclusions in the paper are present in the paper and/or the Supplementary Materials. Additional data related to this paper may be requested from the authors.

Submitted 18 January 2020
Accepted 2 June 2020
Published 15 July 2020
10.1126/sciadv.aba9589

Citation: B. B. Li, E. Y. Scott, M. D. Chamberlain, B. T. V. Duong, S. Zhang, S. J. Done, A. R. Wheeler, Cell invasion in digital microfluidic microgel systems. *Sci. Adv.* **6**, eaba9589 (2020).